Key Points:

- The topography in the Grimsel region drives meteoric water to depths exceeding 10 km, causing discharge of thermal water at Grimsel Pass
- Based on thermal and chemical constraints from the spring water, the bulk fault permeability is in the range of 2e−15 m^2–4.8e−15 m^2
- Recent periods of glaciation changed the pattern of flow in the fault plane and are likely the reason for fluid residence times >30,000 years

Correspondence to:
P. Alt-Epping,
alt-epping@geo.unibe.ch

Permeability and Groundwater Flow Dynamics in Deep-Reaching Orogenic Faults Estimated From Regional-Scale Hydraulic Simulations

Peter Alt-Epping[1] ID, Larryn W. Diamond[1] ID, and Christoph Wanner[1] ID

[1]Rock-Water Interaction Group, Institute of Geological Sciences, University of Bern, Bern, Switzerland

Abstract Numerical modeling is used to understand the regional scale flow dynamics of the fault-hosted orogenic geothermal system at the Grimsel Mountain Pass in the Swiss Alps. The model is calibrated against observations from thermal springs discharging in a tunnel some 250 m underneath Grimsel Pass to derive estimates for the bulk permeability of the fault. Simulations confirm that without the fault as a hydraulic conductor the thermal springs would not exist. Regional topography alone drives meteoric water in a single pass through the fault plane where it penetrates to depths exceeding 10 km and acquires temperatures in excess of 250°C. Thermal constraints from the thermal springs at Grimsel Pass suggest bulk fault permeabilities in the range of 2e−15 m^2–4.8e−15 m^2. Reported residence times of >30,000 and 7 years for the deep geothermal and shallow groundwater components in the thermal spring water, respectively, suggest fault permeabilities of around 2.5e−15 m^2. We show that the long residence time of the deep geothermal water is likely a consequence of low recharge rates during the last glaciation event in the Swiss Alps, which started some 30,000 years ago. Deep groundwater discharging at Grimsel Pass today thus infiltrated the Grimsel fault prior to the last glaciation event. The range of permeabilities estimated from observational constraints is fully consistent with a subcritical single-pass flow system in the fault plane.

Plain Language Summary Observations from warm springs discharging through a fault at Grimsel Pass (2,164 m.a.s.l.) in the Swiss Alps are used to constrain a numerical model of the deep water circulation feeding the springs. The springs are known to have been active for at least 3.3 million years and to be due to ascent of meteoric water that penetrated to depths exceeding 10 km, where it acquired temperatures above 250°C. Simulations show that the circulation along the fault connects a meteoric recharge zone at high altitude to the west with a sub-vertical permeable discharge zone at Grimsel Pass. A key unknown is the permeability of the fault. Temperature, discharge rate and chemical composition of the spring water depend on flow conditions at depth and can be used to estimate the fault's bulk permeability. Our study shows that the range of fault permeabilities can be narrowed down to roughly half an order of magnitude: 1e−15 m^2–5e−15 m^2. This permeability range is consistent with a currently stable, single-pass flow pattern. Long water-residence times inferred from the isotopic composition of the spring water suggest low recharge rates during the last glaciation and the dominance of a multi-pass flow pattern during that time.

1. Introduction

In low-permeability crystalline rocks, fractures and faults exert a prime influence on the flow of groundwater (and other crustal fluids not considered here) and hence on the heat and solute mass that it transports. In order to understand the dynamics of regional groundwater flow, it is necessary to know the general permeability structure of the fault zones in that region. Depending on the permeability of the fault in relation to that of the host rock, a fault may either act as a conduit or a barrier to flow.

Regional faults acting as permeable conduits focus regional flow. As a result, chemical reactions between the migrating fluid and the rock may lead to distinct mineral alteration patterns in the rock that may in turn affect fault mechanics (e.g., Bruhn et al., 1994; Wintsch et al., 1995). When flow has ceased, these alteration patterns provide a fossil record of fluid circulation (e.g., Balsamo et al., 2013; Mozley & Goodwin, 1995). Localized mineralization or fluid mixing along faults zones can in some instances lead to the formation of economic mineral deposits (e.g., Garven et al., 1999; Ingebritsen & Appold, 2012; Person et al., 2008) or diagenesis (Chan et al., 2000; Eichhubl et al., 2009). Deeper faults (>1 km) are sometimes associated with hot springs along the fault trace providing evidence for focused advective heat transport (e.g., Bächler et al., 2002; Taillefer et al., 2017).

In contrast, faults my also act as barriers to flow where the permeability along the fault zone can be reduced due to cataclasis, clogging by particles, dissolution/cementation reactions (e.g., the growth of authigenic clay minerals), the regional stress field or other mechanisms (e.g., Bense et al., 2013). In some cases, these faults affect hydrocarbon migration and entrapment in reservoir rocks (e.g., Aydin, 2000). Finally, when fault zones contain both hydraulically active and inactive segments they may constitute complex conduit–barrier systems (e.g., Bense & Person, 2006). Whether a fault zone acts as a conduit, barrier, or combined conduit–barrier system is controlled by the distribution and hydraulic properties of fault core and damage zone structures and by the inherent magnitude and variability of rock-matrix and fracture permeability. Dynamic deformation conditions and chemical changes may be additional controls (Caine et al., 1996; Caine & Minor, 2009).

In collisional orogens, such as the European Alps, steep fault zones are common structural features. Owing to relatively strong hydraulic gradients imposed by the surrounding topography and to the depths of 10 or more kilometers to which these faults zones reach, fluids migrating along these permeable pathways may encounter rocks at temperatures which elsewhere are found only in regions of active magmatic activity. Deep orogenic faults are thus predestined to host natural geothermal systems where hot fluids ascend to the surface. Such orogenic geothermal systems in amagmatic regions have been reported from the Canadian Rocky Mountains (Grasby et al., 2016; Grasby & Hutcheon, 2001), the Southern Alps of New Zealand (Menzies et al., 2014; Reyes, 2015; Reyes et al., 2010), the central European Alps (Diamond et al., 2018; Pfeifer et al., 1992; Sonney & Vuataz, 2008, 2009, 2010; Wanner et al., 2019), the Qilian Mountains of western China (Stober et al., 2016), Taiwan (Upton et al., 2011) and the Himalayas (Craw et al., 2005; Hochstein & Yang, 1995).

The objective of this study is to use hydraulic, thermal and chemical data from thermal springs at Grimsel Pass, a mountain pass at an elevation of 2,164 m a.s.l in the Swiss Alps, to construct a constrained numerical model that provides insight into the hydrogeology of a large, orogenic fault zone. We use an integrated modeling approach to estimate its bulk fault permeability, flow rates within the fault, the depth of fluid circulation and the temperatures encountered by the circulating fluid. Finally, we assess the effect of climatic changes during the Pleistocene on residence times and patterns of flow in the fault. This study essentially integrates the modeling by Wanner et al. (2019), which examined thermal anomalies and the potential for geothermal exploitation induced by thermal upflow at Grimsel Pass, into a regional scale model that tracks the fate of the circulating fluid from the recharge site to the discharge site.

The thermal waters discharge at low rates in a tunnel hosting a trans-European pipeline for natural gas some 250 m underneath Grimsel Pass. These thermal springs are the highest known in the Alps (Hofmann et al., 2004). Diamond et al. (2018) proposed a conceptual model of the flow system in which water infiltrates a permeable fault zone at high altitude >10 km to the west of Grimsel Pass, then penetrates to depths exceeding 10 km and rises back to the surface along a permeable fault linkage zone at Grimsel Pass. This permeable upflow zone is intersected by the tunnel, causing seepage of thermal waters. Thermal, hydraulic, isotopic and geochemical data from these springs provide constraints for numerical models that can be used to assess the bulk permeability of the fault and hydraulic conditions within the fault plane.

2. The Orogenic Hydrothermal System at Grimsel Pass, Switzerland

Grimsel Pass is situated on a long, E–W-trending ridge at the boundary between the Cantons of Bern and Valais in the north and south, respectively. This ridge forms an important water divide with the river Rhône originating south of the Pass and draining into the Mediterranean Sea, and the river Aare originating in the north and draining via a merger with the river Rhine into the North Sea. The mountains toward the west of Grimsel Pass increase steadily in height, exceeding 3,500 m over a distance of several tens of kilometers (Figure 1a). Superimposed on this gradual increase in surface elevation are local peaks and valleys such as the Sidelhorn (2,764 m a.s.l.), some 2 km to the west of Grimsel Pass (Figure 1a).

The bedrock making up the Grimsel ridge is entirely crystalline, consisting of a sequence of granitoids and quartz-ofeldspathic gneisses of high metamorphic grade (Figure 2). These rocks are components of the Aar Massif, a huge block of pre-Triassic European continental basement that was involved in the Paleogene Alpine collisional orogeny and exhumed along steep reverse faults in the Neogene (Herwegh et al., 2017).

Several thermal springs are exposed along a short (<100 m) section of the tunnel underneath Grimsel Pass. Water discharges at rates of 1–4 L/min and at temperatures up to 28°C (Pfeifer et al., 1992; Waber et al., 2017).
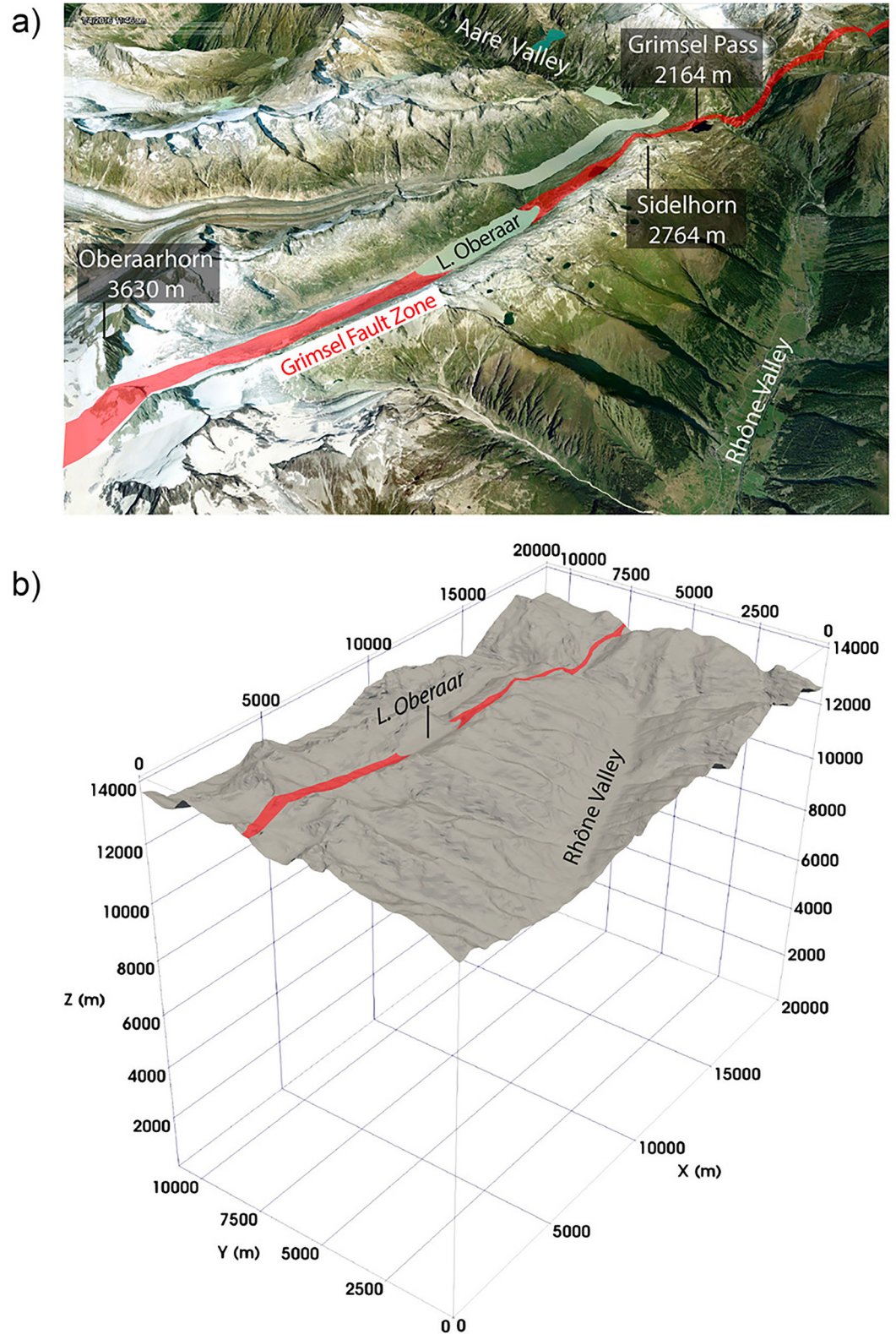
Figure 1. (a) Topography and regional landmarks mentioned in the text looking NE. (b) Surface and dimensions of the model domain.
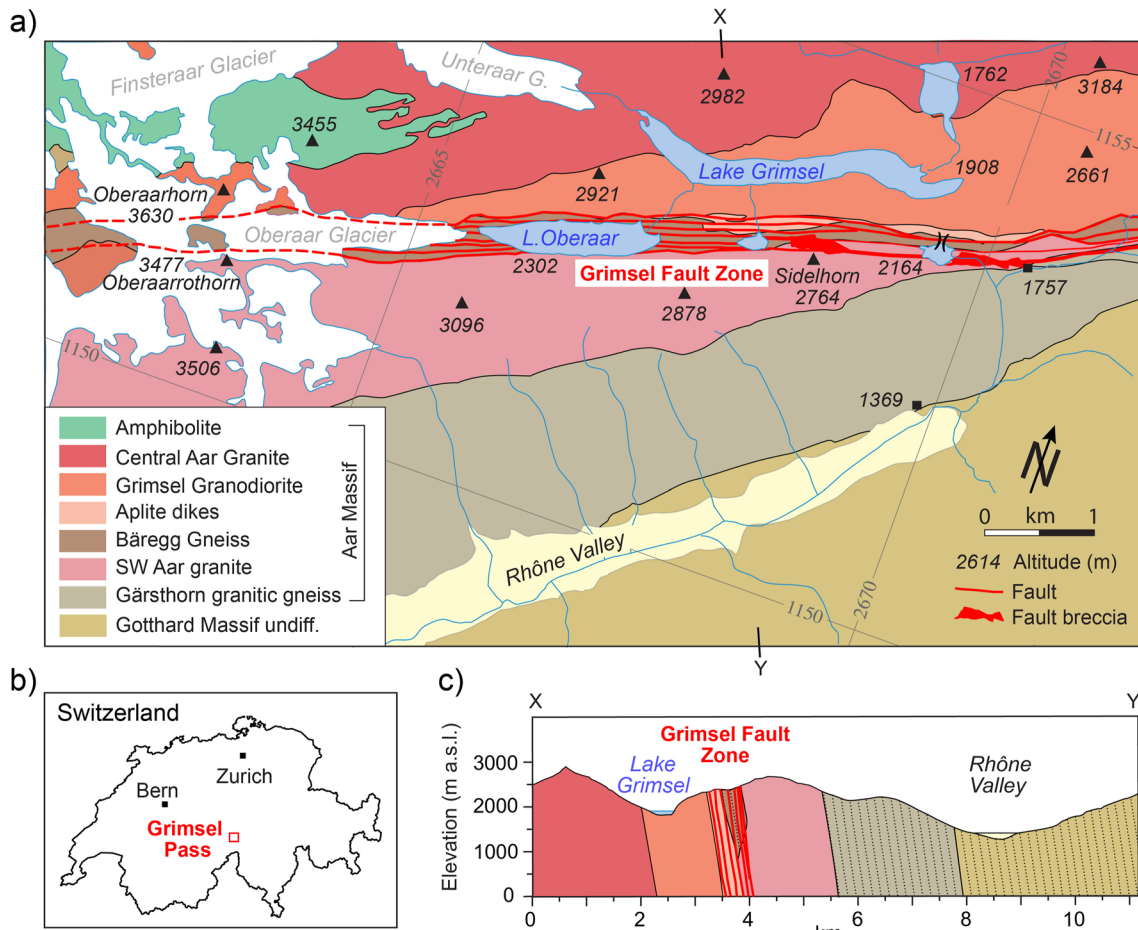
Figure 2. Geological setting of the Grimsel Fault Zone, through which warm water discharges in a tunnel ~250 m below Grimsel Pass. Based on Belgrano et al. (2016) and Berger et al. (2017). (a) Geological map. Coordinates are Swiss km grid. (b) Location of Grimsel Pass in Switzerland. (c) Cross-section X–Y through map. Note different horizontal and vertical scales.

The estimated total discharge in the tunnel amounts to 2–8 L/min (Diamond et al., 2018; Pfeifer et al., 1992). Discharge occurs where the tunnel intersects a major brecciated fault zone which is part of the larger Grimsel Breccia Fault (GBF), a late Neogene ENE-trending strike-slip fault with near-vertical dips of 90° ± 5° (Belgrano et al., 2016) (Figure 2). The GBF itself is part of the Grimsel Fault Zone (Figures 2a and 2c), a larger set of major ENE-trending faults that extend along strike over at least 50 km and to depths of >20 km (Belgrano et al., 2016; Herwegh et al., 2017). Numerous older ductile, mylonitic shear zones run parallel to and are overprinted by the brittle faults (Egli et al., 2018). The breccia zone of the GBF is a subvertical, pipe-like structure. It constitutes a purely brittle, permeable linkage zone between subparallel segments of the main fault zone (red area in Figure 2a). Another such linkage zone is exposed at the surface in the Sidelhorn area to the west (Belgrano et al., 2016) but no recent hydrothermal discharge is known from that site.

Approximately 1 km to the east of Grimsel Pass the GBF passes through a topographic low at about 150 m lower altitude than the springs in the tunnel beneath the Pass. There is no indication of hydrothermal discharge at this low point, suggesting that east of the Pass fluid flow along the fault is inhibited, possibly due to lack of extensional brittle deformation or clogging by clay-bearing gouge (e.g., Morrow et al., 1984). In contrast, the discharge of thermal springs at the Pass demonstrates that the GBF acts as a permeable hydraulic conductor over large distances along the Grimsel ridge toward the west of the Pass. Thus, the paradoxical discharge of thermal water in the tunnel directly below the mountain Pass, rather than in the deep valleys to the north or south, is clear field evidence of a strong permeability contrast between the fault and its crystalline host rocks. Outcrops of the host rocks are nevertheless fractured. Erosional unloading has produced abundant exfoliation joints down to a depth of 200 m (Ziegler et al., 2013), and in the Aare Valley 3 km north of Grimsel Pass, subvertical fractures

permit infiltration of meteoric water over large areas down to 400 m depth (Keusen et al., 1989). To explain the paradoxical lack of N–S hydraulic connectivity below the Grimsel Pass tunnel, it can be inferred that permeable fracture networks are absent below 250 m depth.

Near-surface hydraulic tests within a borehole through the breccia zone (the upflow zone) confirm a relatively high permeability of about 1e−13 m^2 (Cheng & Renner, 2018). The porosity of the upflow zone has been estimated from the borehole televiewer logs (Egli et al., 2018) to be around 0.04 (Wanner et al., 2019). The permeability of the surrounding undisturbed granite is 3e−20 m^2 and its porosity is around 1% according to measurements in the nearby Grimsel Test Site underground laboratory (Bossart & Mazurek, 1991; Ota et al., 2003). The abundant mylonitic shear zones that run parallel to the GBF on both its northern and southern sides have permeabilities of 6e−20 m^2 along to their foliation and 3e−21 m^2 perpendicular to their foliation (Wenning et al., 2018). At depths greater than 250 m, where the low-permeability host rock is intact, these mylonites presumably serve as highly impermeable screens, precluding fluid flow perpendicularly from the fault plane toward the north and south.

It is well known that bulk permeability generally decreases with depth (Ingebritsen et al., 2006; Stober & Bucher, 2007). The higher permeability near the surface is generally attributed to enhanced brittle fracturing. A limit to the depth of groundwater flow is imposed by the transition to ductile fault rheology, which in the quartz-rich host granites and gneisses of the Aar Massif occurs at about 310°C (Stöckhert et al., 1999). Given that there is no magmatic heat source in the Central Alps, the estimated local geothermal gradient for the Grimsel region of 25°C/km (Vernon et al., 2008, 2009) limits the depth of meteoric infiltration to about 12 km. This depth estimate coincides well with the focal depths of earthquakes along the trend of the GBF, the great majority of which are shallower than 12 km (Diehl et al., 2021 and references therein; Belgrano et al., 2016). There are no data on the depth dependency of permeability for the granitic host rock nor for the hydraulically active segment of the Grimsel fault. However, the isotopic composition of the spring water suggests that mixing between hot deep geothermal water and cold shallow groundwater occurs at ratios of about 1:1 (Waber et al., 2017). Whether this can be used as evidence for enhanced permeability at shallow depth will be assessed in numerical simulations presented below.

Fluid flow through the GBF is known to have been active intermittently for at least 3.3 Ma (Berger et al., 2022; Hofmann et al., 2004). Water residence times estimated from tritium and ^{14}C data are at least 30 ka for the deep geothermal waters and about ∼7 years for the shallow cold waters (Waber et al., 2017). The δ^{2}H and δ^{18}O values of the thermal springs fall on the local meteoric water line and are consistent with current rainfall. This indicates that meteoric water is recharging the geothermal system and that recharge occurred at times where the climatic conditions were similar to those of today (Waber et al., 2017). Moreover, the thermal springs show more negative δ^{2}H and δ^{18}O values than the nearby cold-water springs, suggesting that the source of the thermal water is from an infiltration site at higher altitude than Grimsel Pass (Waber et al., 2017). Isotope data suggest that the site of meteoric infiltration could have been around 850 m higher than Grimsel Pass (Wanner et al., 2019). Given the regional topography, this places the recharge site somewhere in the high mountainous terrain to the west of the Pass (Figure 1a).

Diamond et al. (2018) estimated a minimum temperature of 211°C for the deep thermal end-member water, based on Na/K ratios in the spring water. They argued that the maximum water temperature is probably in the range of 230–250°C, possibly even higher. Given the local geothermal gradient of 25°C/km, the temperature values constrain the depth of circulation to a minimum of about 8.5 km but more likely to at least 10 km (Diamond et al., 2018; Wanner et al., 2019).

Because of the high altitude of Grimsel Pass and the mountains surrounding it, meteoric recharge into the subsurface was affected by multiple glaciation events during the Pleistocene. These periods of glaciation alternated with interglacial/interstadial periods when glaciers retreated from the foreland into the highest mountain areas and regions previously covered with ice became exposed to melt- and rainwater infiltration. The residence time of >30 ka points to meteoric infiltration of the current thermal spring water prior to the last glaciation, possibly during the Middle Birrfeld interstadial period or during an even older interglacial period when significant meteoric recharge into the system was possible (Dzikowski et al., 2016; Maréchal et al., 1999; Thiebaud et al., 2010). The last glaciation event (Birrfeld Glaciation) began some 30,000 years ago and ended with the beginning of the Holocene epoch about 11,500 years ago. Throughout most of the Holocene the Grimsel region has been free of permanent ice and exposed to rainfall and meltwater infiltration during the warm months of the year. Current recharge into the fault plane may still be affected by permafrost that is common in the Swiss Alps at elevations

above about 2,500 m. The distribution of permafrost is dependent on various factors, such as the mean ground surface temperature, which in turn is affected by solar radiation, the depth and duration of snow cover, and the geothermal gradient. Its depth ranges from a few tens of meters to hundreds of meters in the highest terrain. Given the complex Alpine topography and climate history, the distribution of permafrost varies in space and time (Noetzli & Phillips, 2019). It is unlikely that permafrost completely inhibits recharge into the deep groundwater system, but it may add heterogeneity to the shallow recharge zone due to local clogging of fluid pathways by ice.

Alt-Epping et al. (2021) performed numerical simulations to investigate the role of such climate-induced variability of recharge on the patterns of fluid flow within a generic fault patterned on the GBF. They concluded that deep-reaching single-pass flow (as is happening today in the GBF) typifies an interglacial period, characterized by high meteoric recharge into the fault (more than several tens of cm/m^2 per year) at flow conditions equal to or slightly lower than the critical Rayleigh number. Further, they found that flow to a given penetration depth (e.g., 10 km) can only be achieved if the fault plane is hydraulically conductive over a matching horizontal extent (e.g., 10 km) toward higher terrain. These conditions constrain the bulk fault permeability to <1e−14 m^2. Conversely, a layered flow regime results from the modest recharge associated with Pleistocene glaciation events, such that single-pass flow occurs only at shallow depths while non-Rayleigh convective flow occurs deep in the fault. Similar layered flow arises if the length/depth ratio of the hydraulically connected region of the fault is low and when flux through the fault is limited by the area of the recharge zone.

3. Model Construction

We use the open source, massively parallel subsurface flow and reactive transport code PFLOTRAN (Hammond & Lichtner, 2010; Hammond et al., 2014; www.pflotran.org) to carry out simulations of regional scale hydrothermal circulation at the Grimsel Pass. The size of the model domain is 20 km × 11 km in the horizontal directions (Figure 1b). The bottom of the domain is set to be 12.5 km below the lowest point of the topographic surface. We use a structured grid to discretize the domain into 3.9 million cells. Hydraulic gradients present near fault zones must be taken into account in order to accurately simulate flow conditions within the fault. Hence, the top model boundary is an exact representation of the surface relief of the Grimsel region (Figure 1b). The surface is sculptured by deactivating cells above the surface elevation at given *x,y* coordinates.

The Grimsel fault is numerically rendered as a vertical, 100 m wide, roughly E–W trending plane that extends along the long-axis of the domain. The upflow conduit at Grimsel Pass extends from the bottom of the domain to the ground surface and has a cross sectional area of 100 m × 100 m, consistent with the model of Wanner et al. (2019). The width of the fault and the cross-sectional area of the upflow conduit are estimates based on the extent of thermal discharge along the tunnel. In line with the above-mentioned features of the GBF east of Grimsel Pass (Section 2), we assume that there is no flow in the fault plane east of the upflow conduit.

Owing to its small size in comparison to the model resolution, the tunnel beneath the Grimsel Pass is not included in the model. Moreover, because the tunnel is a relatively recent perturbation of the natural fluid pressure field and residence times are on the order of >30,000 years, it is not likely to have an effect on the regional deep flow system at this point in time. It therefore seems reasonable to neglect the effect of the tunnel for the purpose of assessing conditions on a system scale.

The host rock is assumed to have a homogeneous and isotropic permeability of 3e−20 m^2 (Ota et al., 2003) and a porosity of 0.01 (Bossart & Mazurek, 1991). This low permeability corresponds to the measured matrix permeability. Additional simulations are carried out to assess the impact of higher, fracture-induced host rock permeabilities. The brecciated zone constituting the upflow conduit is assumed to have a homogeneous and isotropic permeability of 1e−13 m^2 and a porosity of 0.04 (Wanner et al., 2019). The porosity of the fault plane itself is not known. We assume somewhat arbitrarily a porosity of 0.035 for all permeability cases. There are some uncertainties related to the choice of porosity as there is significant spatial variability. For instance, Egli et al. (2018) measured much higher porosities (>20%) in a relatively narrow (∼5 m) "fault core" within the upflow conduit some 115 m below the surface. Moreover, in reality porosity and permeability tend to be correlated. This correlation is neglected here for simplicity. The role of the porosity and the implications of uncertainties related to spatial variability will be included in the discussion where necessary.

The simulated time period of all calculation cases is 300,000 years. This period covers only a fraction of the age of the system (at least 3.3 Ma) but it is long enough to attain steady-state flow and temperature conditions.

Table 1
Material Properties

	Fault	Conduit	Basement rock
Permeability (m²)	1e−15 m²–1e−14 m²	1e−13 m²	3e−20 m²
Porosity	0.035	0.04	0.01
Thermal conductivity (W/(K m))	3.34	3.34	3.34
Heat capacity (J/(K kg))	800	800	800
Van Genuchten *alpha* (1/Pa)	1e−4	1e−4	1e−4
Van Genuchten *m*	0.5	0.5	0.5

Infiltration is modeled as a Neumann flux, superimposed onto a combined conductance and Dirichlet boundary condition. Details of these superimposed boundary conditions can be found in Alt-Epping et al. (2021). The temperature along the topographic surface is fixed at 5°C. We ignore the fact that the air temperature changes with altitude, because the thermal gradient in air is much lower than the geothermal gradient (the adiabatic lapse rate amounts to about 5.5°C/km). We also ignore the fact that the average air temperature may have changed during glacial and interglacial periods.

All side boundaries of the model are impermeable and adiabatic. A constant heat flux is assigned to the bottom boundary resulting in a background vertical thermal gradient of 25°C/km. Thermal and hydraulic properties of the different materials are summarized in Table 1.

4. Results

4.1. No Fault

To assess the role of the fault plane on the regional flow system we first assume a model scenario in which the upflow conduit is present but the fault is absent. The questions we address with this scenario are whether there is sufficient permeability and the necessary hydraulic driving force in the surrounding rocks to sustain fluid upflow at Grimsel Pass without the fault. Simulations were carried out for two rock permeabilities, 3e−20 m² and 1e−17 m², to represent conditions of uniform matrix permeability on the one hand, and enhanced permeability due to ubiquitous fracturing on the other. The results show that over this permeability range, fluid flow is too weak to sustain upflow of deep geothermal water along the full vertical length of the conduit. In fact, cold surface water infiltrates into the conduit at the surface leading to slow downward flow at shallow depth. The flow rates through the rock are too low to sustain upflow along the conduit, which is consistent with insights from other studies that permeabilities lower than 1e−16 m² entail conduction-dominated heat transport for most plausible upper-crustal conditions (e.g., Manning & Ingebritsen, 1999; Norton & Knight, 1977).

Nevertheless, even at very low permeabilities, groundwater is not entirely stagnant and there exists a regional flow pattern albeit at very low flow rates. This regional flow pattern is controlled by the topography, whereby the "wavelength" and "amplitude" of elevation highs and lows determine the depth and direction of flow. Local scale, low amplitude hill-and-valley topography controls flow at shallow depth. Meteoric water infiltrating at high altitude west of Grimsel Pass penetrates much deeper into the rock, reaching depths of several kilometers. Under homogeneous permeability conditions, most of this deep groundwater flow follows the topographic gradients and drains into the Rhône Valley south-west of Grimsel Pass, which constitutes the regional elevation minimum (Figure 3). The upflow conduit, despite having a several orders of magnitude higher permeability, has no impact on the regional-scale deep groundwater flow pattern.

4.2. The Grimsel Fault as a Hydraulically Active Structure

We use the same model as in Section 4.1 but add the Grimsel fault as a 100 m wide, permeable vertical plane, connecting the glaciated mountains in the west with the vertical upflow conduit at Grimsel Pass. The infiltration of meteoric water into the fault plane is controlled by its permeability, the cross-sectional area of the recharge zone and the surrounding topography. It is not limited by the supply of rain- or meltwater. Generic insights from Alt-Epping et al. (2021), suggest that a fault permeability range of 1e−15 m² to 1e−14 m² is needed to achieve a
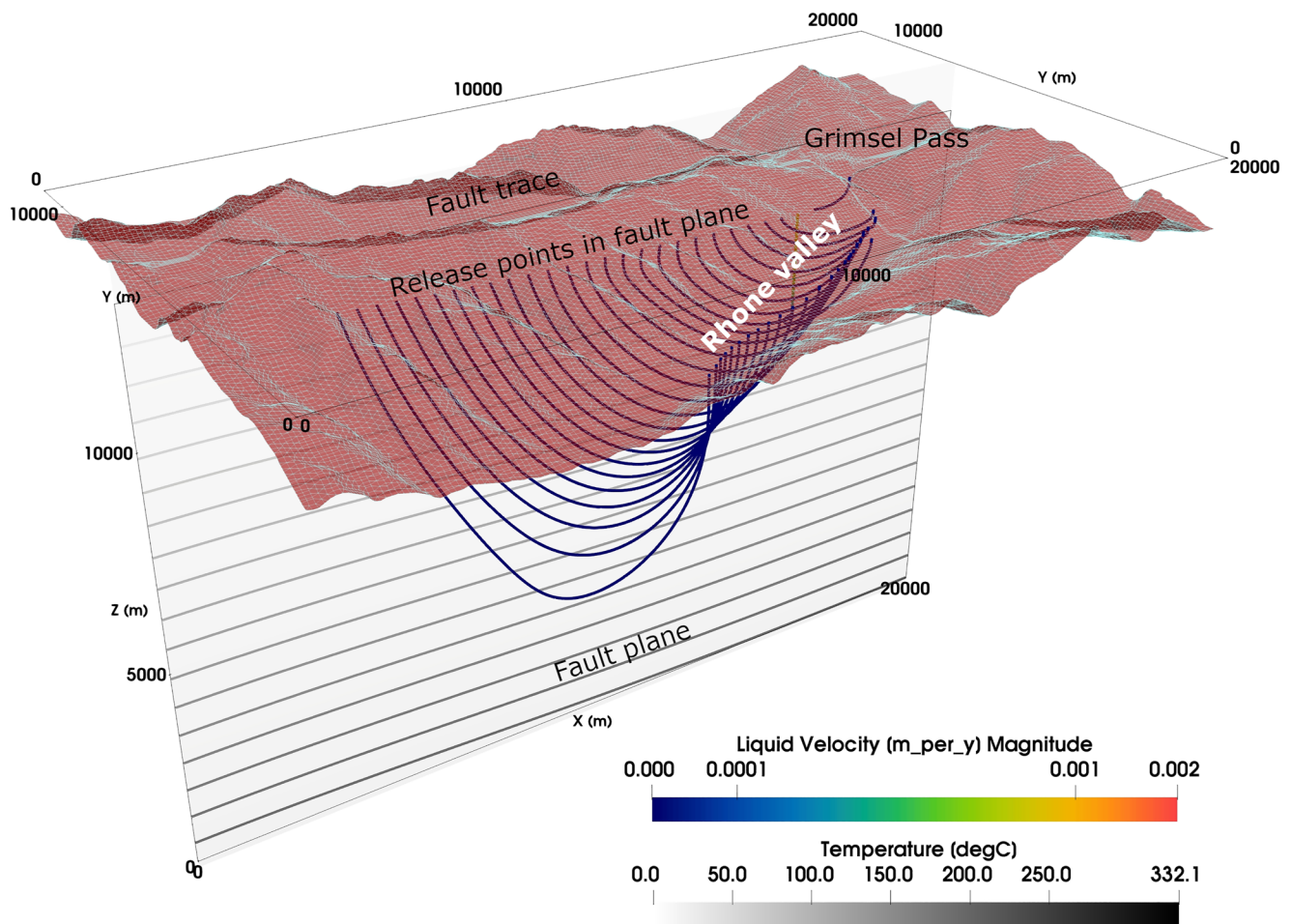
Figure 3. View of model domain toward NE. Temperature contours show conductive conditions with slightly elevated isotherms toward the west. Streamlines of tracers released along the fault plane (which in this simulation has the same low permeability as the surrounding rock) showing the deep flow pattern in the Grimsel region. All the deep groundwater discharges into the river Rhône SW of Grimsel Pass. The Rhône valley constitutes the regional topographic low.

stable, thermally effective single-pass flow pattern. Values below this range result in conduction whereas those above result in flow dominated by free convection. In this study we narrow down this range further by using constraints from the real geothermal system.

Using a fault permeability of $k_{fault} = 1e{-}15$ m^2, a single-pass flow-through system evolves where meteoric water penetrates to a depth exceeding 10 km and ascends to the surface through the upflow conduit at Grimsel Pass (Figure 4a). Along its loop through the plane, the water attains temperatures exceeding 300°C. The flow pattern and maximum temperature are consistent with the conceptual model of Diamond et al. (2018) and confirm the essential character of the Grimsel fault as a permeable groundwater conductor hosting a deep groundwater circulation system.

Flow rates within the fault plane are generally low at $<3e{-}2$ m^3 m^{-2} yr^{-1}. Inflow from the fault into the conduit under Grimsel Pass occurs throughout its vertical extent, decreasing slightly from bottom to the top of the conduit. As a result of continuous lateral inflow, the vertical flux along the conduit increases toward shallower depths to values of up to 2.5 m^3/m^{-2} yr^{-1} at the depth of the tunnel. Integrated over the cross-sectional area of the model conduit this amounts to a flux of 44 l/min (Table 2).

Increasing the fault permeability to $k_{fault} = 5e{-}15$ m^2 yields a single-pass flow pattern with stronger vertical flow components in the recharge zone and near the discharge conduit, indicating that buoyancy becomes an additional driving force for flow (Figure 4b). Stronger lateral flow into the conduit increases the vertical flux, resulting in
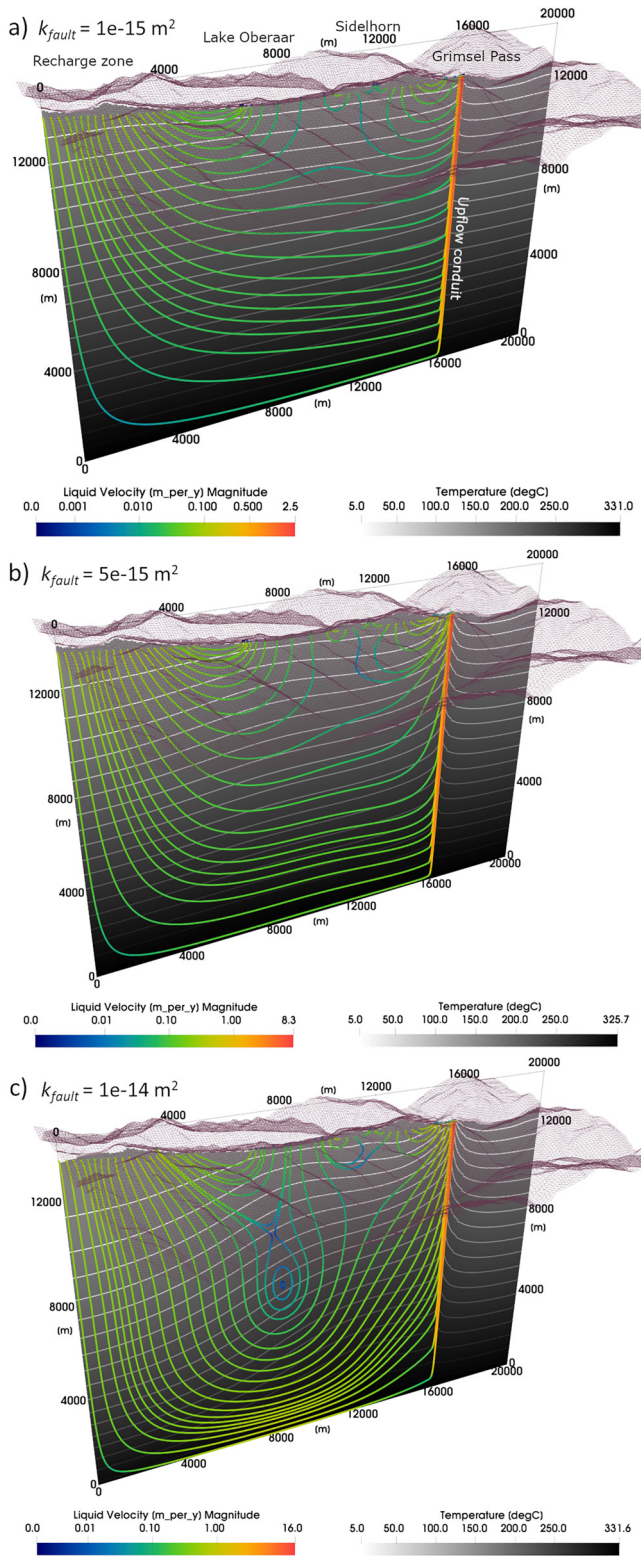
Figure 4. View of model domain to the NE. No flow occurs to the east of the upflow conduit at Grimsel Pass, consistent with field observations given in the text (Section 2). Flow field and temperature distribution are shown for three different fault permeabilities: (a) 1e−15 m², (b) 5e−15 m² and (c) 1e−14 m². Permeability of host basement rock is 3e−20 m² (Table 1).

a total discharge at the depth of the tunnel of 144 L/min. This is a factor 3.3 higher compared to a fault permeability $k_{fault} = $ 1e−15 m².

By increasing the fault permeability to 1e−14 m², the flux in the deep fault becomes more than an order of magnitude higher than at $k_{fault} = $ 1e−15 m² (Figure 4c). A small convection cell forms at about mid-depth, indicating that buoyancy starts to overprint topography-driven flow. Within the conduit the vertical flux and the total discharge increase further, resulting in a flux of 270 L/min at the depth of the tunnel. Aside from a stronger upflow within the conduit there is also a significant vertical flow component within the fault plane immediately outside the conduit with flow rates on the order of 0.35–0.4 m³ m⁻² yr⁻¹. This broad zone of fluid upflow contrasts with the more focused upflow along the conduit at lower fault permeabilities (Figures 3a and 3c). Apart from buoyancy, broad vertical upflow extending beyond the conduit is enhanced because, with increasing fault permeability and decreasing permeability-contrast, the conduit loses its focusing character. Ultimately, by increasing the fault permeability further, the conduit would become just an extension of the fault plane and fluid upflow would no longer be focused under Grimsel Pass.

Common to all flow patterns shown in Figure 4 is that the depth of infiltration increases with the distance from the discharge zone and hence with increasing altitude of the recharge zone. It is not known how far the hydraulically active part of the fault extends to the west. Given that the surface elevation increases beyond the model boundaries, it is possible that fluid circulation may be even deeper provided that brittle conditions still exist at that depth. Superimposed on the deep flow system is shallow groundwater flow driven by local, small-scale hill-and-valley topography. For instance, a local recharge zone in the Sidelhorn area leads to shallow groundwater flow toward Grimsel Pass. This area is one of the potential sources for the shallow groundwater component found in the spring water sampled in the tunnel.

A local discharge area occurs at Lake Oberaar, a dammed lake west of the Sidelhorn mountain (Figures 1 and 4). Unlike at Grimsel Pass, discharge is more diffuse and occurs at very low rates. It is interesting to note that this discharge area coincides with the origin of the River Aare, one of the biggest rivers in Switzerland. However, given the low discharge rates, it is not likely that there is a significant contribution of groundwater to the river system compared to the direct contribution of rainfall and meltwater.

4.3. Comparing Model Results With Observational Constraints

4.3.1. Flow Rates

In the real system the estimated total discharge of all springs in the tunnel amounts to about 2–8 L/min. Given that the upflow zone extends beyond the bounds of the narrow, 3 m diameter tunnel and that an unknown fraction of the upwelling water bypasses the tunnel, the stated discharge is probably a strong underestimate of the real flux along the conduit. Hence, it is to be expected that the fluxes predicted by the model are much higher (Table 2). Furthermore, the unknown effect of the tunnel as a low pressure anomaly makes it difficult to compare the real and modeled systems based on total fluxes. Nevertheless, the broad agreement between the observed and modeled fluxes confirms that the assumed range of fault permeabilities is realistic, although the flux is clearly not a suitable parameter to narrow down that range any further.

Table 2
Summary of System Characteristics Used as Calibration Targets as a Function of the Fault Permeability

Fault permeability (m^2)	Total discharge at tunnel depth (L/min)	Average/max temperature at tunnel depth (°C)	Residence time (years)	Average/max fraction shallow groundwater (%)
1e−15	44	20.4/23.2	22,900	17.7/53.2
5e−15	144	52.1/55.1	6,300	2.2/7.9
1e−14	270	82.1/87.3	4,000	0.16/0.6

4.3.2. Mixing Ratios

Throughout the tested permeability range 1e−15 m^2–1e−14 m^2, there is continuous lateral flow into the conduit that adopts a progressively more vertical flow direction as permeability increases (Figure 3). The flow pattern shows deep geothermal water rising from the deep fault and mixing with shallow groundwater recharging primarily in the Sidelhorn area. Mixing of deep and shallow water is consistent with the isotope signature of the waters sampled in the tunnel. However, these signatures suggest mixing ratios of about 1:1.

To quantify mixing ratios between deep and shallow water components in the simulation, we couple the flow system with tracer transport. Two tracers are used to track and distinguish circulating water based on the region of infiltration: one tracer tracks infiltration at high altitude between the western boundary of the model and the region of groundwater discharge at Lake Oberaar, the other tracer tracks infiltration between Lake Oberaar and the upflow conduit at Grimsel Pass. Assuming plug flow and neglecting dispersion and diffusion, mixing ratios of the tracers at the depth of the tunnel yield the fractions of deep and shallow groundwater in the spring water.

Note that the upflow conduit is internally discretized and mixing between deep and shallow water varies across the cross-sectional area of the conduit. In the model this heterogeneous distribution is primarily controlled by the fact that inflow into the conduit occurs from the fault plane and there is relatively little lateral mixing taking place within the conduit as the flow direction is essentially vertical. This spatial variability is also expected to occur in the real system, although it is probably more complex in its pattern and unpredictable in its nature owing to internal hydraulic heterogeneity and tortuous flowpaths within the conduit. To account for spatial heterogeneity we report in Table 2 the average tracer concentrations integrated over the cross-sectional area of the conduit as well as the local concentration maxima.

The results show that on average the fraction of shallow water is lower than 50% for all permeabilities and becomes extremely low as the fault permeability increases (Table 2). Only in the spatially resolved mixing ratios at k_{fault} = 1e−15 m^2 is the fraction of shallow groundwater as high as 54%, which is in good agreement with observations. The general trend that the fraction of shallow groundwater decreases with increasing permeability is to a large part a consequence of enhanced upwelling of deep water within and, more importantly, around the conduit, inhibiting the inflow of shallow groundwater into the conduit. Given this trend one could infer that the fault permeability is lower than 1e−15 m^2. Alternatively, this discrepancy may point to a process not considered in the current model. Which process this could be will be discussed below.

4.3.3. Residence Times

Simulations coupling flow with tracer transport can also be used to calculate solute residence times. The residence time corresponds to the breakthrough time at the thermal springs of a tracer injected at high altitude west of Grimsel Pass. In the real system this time is >30 ka. The modeled residence time depends on the average linear flow velocity, which means that it also depends on the porosity of the fault plane. Because neither the porosity nor a representative porosity–permeability relationship is known for the rocks of the fault plane, the choice of porosity (here 3.5% at all permeabilities) implies some uncertainty in the computed residence times. These uncertainties will be considered in the following discussion.

The results show that residence times for higher fault permeabilities (5e−15 m^2–1e−14 m^2) are unrealistically short even when uncertainties in porosity are taken into account (Table 2). Assuming that residence times scale linearly with porosity, the porosity would have to be at least a factor of six higher than in the current model to match real residence times. The highest porosity measured for a discrete zone of cataclasites by Egli et al. (2018) is 16%. This is roughly 5 times the value used in the current model. However, given the dimensions of the fault zone (width and depth) and considering that discharge into the tunnel occurs in several springs along a roughly 100 m long segment of the tunnel (Wanner et al., 2019), there is sufficient evidence that upflow is distributed over a relatively broad cross-sectional area and not confined to a single discrete zone of high porosity and permeability. In other words, we consider a porosity of 16% a local extreme measured on a length scale that is smaller than the length scale representing the bulk properties of the rock that determine the average flow and transport
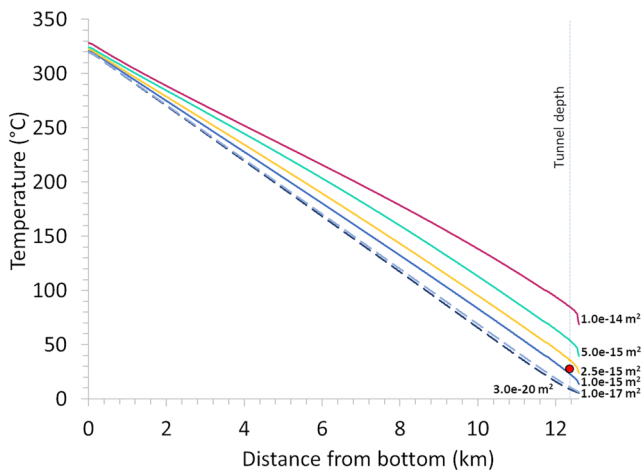
Figure 5. Simulated temperature profiles along the upflow conduit within the fault plane for different fault permeabilities. At permeabilities <1e−17 m^2 the temperature profiles are linear and overlap, indicating conductive conditions. With the onset of convective heat transport the profiles tend toward higher temperatures with increasing permeability. The red dot marks the maximum measured spring water temperature of 28°C at the depth of the tunnel. To match this temperature, the fault permeability has to be between 1e−15 m^2 and 2.5e−15 m^2. However, the temperature profiles at shallow depth are not directly comparable with the observations, because for all fault permeabilities the water at tunnel depth has a fraction of shallow groundwater that is lower than observed.

rates along the upflow zone. This implies that a factor of six higher porosity needed to scale the residence times at high fault permeabilities would be unrealistic.

At the lower end of the permeability range, k_{fault} = 1e−15 m^2 yields a residence time of 23,000 years, which is still too short, but this mismatch could have been caused by underestimating the porosity at this permeability. Alternatively, this mismatch could point to fault permeabilities lower than 1e−15 m^2 or to other processes not considered in the model. A possible reason why the model systematically underestimates residence times will be discussed below.

4.3.4. Temperature

Similar to the tracer mixing ratios, there is spatial variability in the temperature distribution across the cross-sectional area of the conduit and so we report average as well as spatially resolved maximum temperatures (Table 2). This spatial variability is not as significant as that shown by solute concentrations as it is dampened by lateral heat conduction.

All temperature profiles show cooling of the ascending geothermal water owing to conductive heat loss and mixing with shallower water during ascent (Figure 5). For fault permeabilities of 1e−17 m^2 and below, the temperature profile is linear and confirms conduction-dominated heat transport within the permeable conduit. This is consistent with the conclusion from Section 4.1 that without the fault plane the conduit is hydraulically inactive. Conduction alone strongly underestimates temperatures at the depth of the tunnel.

Increasing the fault permeability to 1e−15 m^2 induces upwelling of deep geothermal water along the conduit, raising the average temperature at tunnel depth to 20.8°C and the maximum temperature to 23°C (Table 2). These temperatures are lower than the highest temperature measured at the springs (28°C). A permeability of 2.5e−15 m^2 yields an average temperature of 32.5°C (Figure 5). This indicates that to obtain a temperature of 28°C, the fault permeability must lie between 1e−15 m^2 and 2.5e−15 m^2. Using a high fault permeability of 1e−14 m^2 yields an average discharge temperature at the depth of the tunnel of 80°C, which is unrealistically high.

However, the temperature estimates at tunnel depth reported in Table 2 and shown in Figure 5 have to be viewed with some caution, because these temperatures do not account for the relatively high fraction of the geothermal component in the water at tunnel depth as indicated by the mixing ratios of the tracers. This implies that the simulations overestimate the water temperature at tunnel depth. However, if lateral heat transfer and the temperature dependence of the heat capacity are neglected, it is possible to estimate the temperature of the deep geothermal component alone based on known mixing ratios of deep and shallow water components. This endmember geothermal temperature is solely a function of flow conditions in the fault plane.

Assuming a mixing ratio of 1:1, an average spring-water temperature of 28°C, an average recharge temperature of 5°C (as in the model) and conductive heating in the shallow groundwater system (i.e., a temperature if 11.25°C at the depth of the tunnel), the temperature of the endmember geothermal water is about 45°C. Assuming 5°C for the shallow groundwater water component without conductive heating from the rock (i.e., a temperature of 5°C at the depth of the tunnel) yields an endmember temperature of 51°C. Considering 5°C and 28°C as conservative lower and upper bounds of the recharge and discharge temperature, respectively, a temperature of 51°C poses an upper limit to the temperature of the endmember geothermal water. This upper temperature limit can be used to define a conservative upper bound of the range of fault permeabilities using the relationship between the average endmember temperature and the fault permeability derived from simulations (Figure 6). According to this relationship this upper permeability limit is about 4.8e−15 m^2. Assuming conductive heating of the downwelling shallow groundwater lowers the upper permeability limit to about 4.2e−15 m^2.
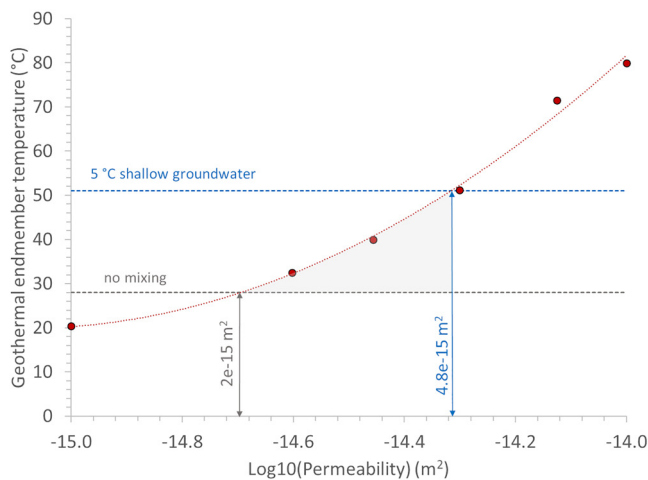
Figure 6. Simulated temperature of the upwelling geothermal endmember water in the springs as a function of permeability. A conservative upper bound of fault permeabilities can be derived from temperature conditions reflecting no heating of shallow groundwater during downflow (i.e., 5°C) and the highest measured spring temperature of 28°C. This upper bound of permeabilities is around $4.8e{-}15$ m^2. A conservative lower bound can be defined by assuming an endmember temperature of 28°C, as if no mixing with shallow water had occurred. This lower permeability limit is around $2e{-}15$ m^2.

A conservative lower bound for the range of permeabilities can be defined by assuming no mixing with shallow groundwater. Without mixing, the endmember temperature corresponds to the spring temperature of 28°C which yields a fault permeability of around $2e{-}15$ m^2 (Figure 6).

5. Discussion

Temperature constraints provide a range of plausible fault permeabilities, $2.e{-}15$ m^2–$4.8e{-}15$ m^2 (Figure 6) that is consistent with a single-pass flow system at subcritical Rayleigh numbers. At subcritical conditions, convective heat transport outweighs conductive heat transport and topography-driven flow dominates over buoyancy-driven flow.

This permeability range supports the assessment inferred from residence times that the fault permeability is not likely to exceed $5e{-}15$ m^2 (Section 4.3.3). However, there remain discrepancies between model results and observations in terms of residence times for permeabilities lower than $5e{-}15$ m^2 and of the fraction of shallow groundwater at the depth of the tunnel. The simulations seem to suggest, as one possible explanation for these differences, permeabilities lower than $1e{-}15$ m^2. This, however, would be in contradiction to the lower permeability limit imposed by temperature constraints. Hence, these discrepancies could be due to processes not considered in the simulations.

The isotopic signature of the spring water suggests a mixing ratio of the deep geothermal water and shallow groundwater of around 1:1 and a residence of the shallow groundwater of about 7 years (Waber et al., 2017). Flow rates (Darcy fluxes) at shallow depth are on the order of cm/yr (Figure 4). Given these low flow rates and taking into account the depth of the tunnel (250 m), it would require unrealistically small porosities to achieve a residence time of 7 years.

It is possible that computed flow rates are too low. As described in Section 2, the upper few hundred meters of the Grimsel bedrock contains fractures. To assess the effect of this relatively permeable layer on flow rates, additional simulations were carried out in which a 400 m thick surface layer with an equivalent porous-matrix permeability of $5e{-}14$ m^2 was added to the 3D model. The depth of 400 m is well below the depth of the tunnel and the permeability of $5e{-}14$ m^2 falls within the range of near-surface permeabilities reported in Ingebritsen et al. (2006). The results show that the fault plane with its lower permeability loses its flow-focusing character for shallow groundwater and, as a consequence, there is a stronger response of shallow flow to local hill-and-valley topography. Overall, there is little impact on the mixing ratio in the conduit, because shallow groundwater flow is primarily directed toward topographic lows and not toward the conduit. Hence, a near-surface layer of pervasively elevated permeability alone cannot explain the inconsistent mixing ratios.

It is possible that the tunnel itself acts as a low pressure anomaly that draws shallow groundwater from above, thereby focusing flow and enhancing flow rates. Although not included in the 3D model, it is possible to demonstrate the effect of the tunnel on the shallow groundwater system in a simple 1D simulation experiment. In this simulation we estimate the permeability needed for meteoric water containing 1 mol/kg of a tracer to flow through a 250 m vertical interval of rock with atmospheric pressure conditions at both ends of the interval, (i.e., the water percolates through the rock by gravity) such that the residence time of the tracer amounts to 7 years. Tracer breakthrough at the tunnel (250 m below surface) is defined by the arrival of 50% of the inlet concentration, that is, 0.5 mol/kg. We assume a constant porosity of 3.5%, the same porosity as for the fault plane in the regional scale model.

Results show that to achieve tracer breakthrough after 7 years, a permeability of about $2.5e{-}15$ m^2 is needed (Figure 7). This permeability is much higher than the permeability of the host rock and falls well into the range of estimated permeabilities for the fault derived from temperature constraints (Figure 6). Although there is some uncertainty in the choice of porosity, the results confirm that shallow groundwater recharge toward the tunnel has to occur through a zone of elevated permeability. Because the permeability of $2.5e{-}15$ m^2 is well within the range of estimated fault permeabilities, the results do not provide clear evidence for a more widespread enhanced
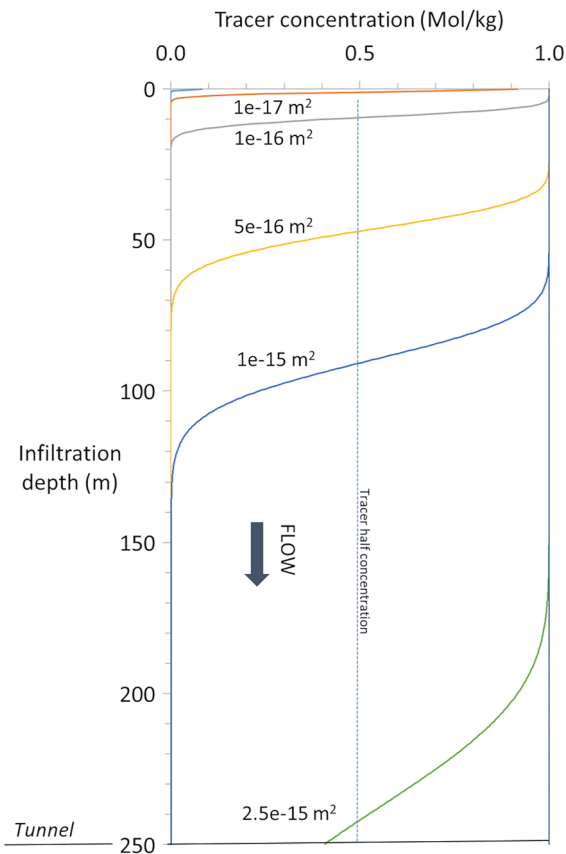
Figure 7. Infiltration depth of a tracer front driven through the fractured host rock by gravity after 7 years for different bulk permeabilities. The depth of the tunnel is 250 m below the surface. Breakthrough of the tracer at the desired time and depth is achieved if the bulk fractured rock has a permeability of about 2.5e−15 m².

permeability, but they cannot rule out this possibility either. Instead, shallow groundwater water could just as well infiltrate the fault trace at and around Grimsel Pass and be drawn toward the tunnel along the fault plane. The setting of the tunnel in a zone of enhanced permeability thus explains the short residence times of the shallow groundwater. However, a more detailed analysis is needed to confirm whether, or under what conditions, this mechanism also leads to the observed mixing ratios between deep and shallow water components. Such an analysis is beyond the scope of this study.

There is also disagreement between the modeled and observed system-scale residence times of >30 Kyr. Modeled residence times are too short for the permeability range considered here (Table 2). While for the lower permeabilities in that range (1e−15 m²–5e−15 m²) it is possible that this mismatch is related to underestimating the porosity of the fault plane, this becomes increasingly unlikely as an explanation for the mismatch at higher permeabilities.

Given the length of the residence time, recharge into the fault plane must have been affected by climatic conditions during the Pleistocene. It is likely that recharge into the fault was lower than today during glaciation events—a process not considered in the simulations presented above. The last period of glaciation during which the Swiss Alps were covered by a thick sheet of ice started some 30,000 years ago and ended about 11,000 years ago. It is reasonable to assume that during peak glaciation, recharge was at a minimum because precipitation fell as snow and there was little if any melting of the ice cap. Alt-Epping et al. (2021) showed that the flow system in the fault responds rapidly (<1,000 years) to such recharge-starved conditions by forming a layered flow system with non-Rayleigh convection in the deep regions of the fault plane and single-pass flow in the shallow regions. Non-Rayleigh convection is driven by lateral temperature gradients induced by large wavelength surface topography at subcritical Rayleigh numbers.

To examine the impact of low recharge conditions on the residence time we carry out simulations covering the last 41,000 years in which recharge into the fault is reduced during a glaciation period lasting 20,000 years. Because the exact recharge history during that period is unknown, the results should be seen as a proof of concept rather than an accurate representation of flow conditions in the past. To monitor residence times, different tracers are injected at different times: (a) a pre-glacial tracer that has circulated in the steady state flow field prior to glaciation, (b) a glacial tracer injected when recharge starts to decrease at the onset of the glaciation event and (c) a post-glacial tracer injected when recharge begins to switch back to today's interglacial conditions. When the glacial tracer is injected, the injection of the pre-glacial tracer ceases. The injection of the glacial tracer stops when the post-glacial tracer is injected. The sequence of events is given in Table 3.

In this example a fault permeability of 1e−15 m² is used. Consistent with the result from Alt-Epping et al. (2021), the single-pass flow system persisting during interglacial conditions collapses into a layered flow system with non-Rayleigh convection in the deep and single-pass flow in the shallow parts of the fault during glaciated conditions (Figure 8a). In the recharge zone, the pre-glacial tracer has been partially displaced by the glacial tracer during the transition from warm to cold conditions but when the flow system changes into a large convection cell during peak glaciation, the influx of the glacial tracer and expulsion of the background tracer ceases. Flow velocities in the convection cell are extremely low, so that the interface between the two

Table 3
Sequence of Events Simulated to Assess Effect of Variable Recharge on Water Residence Time

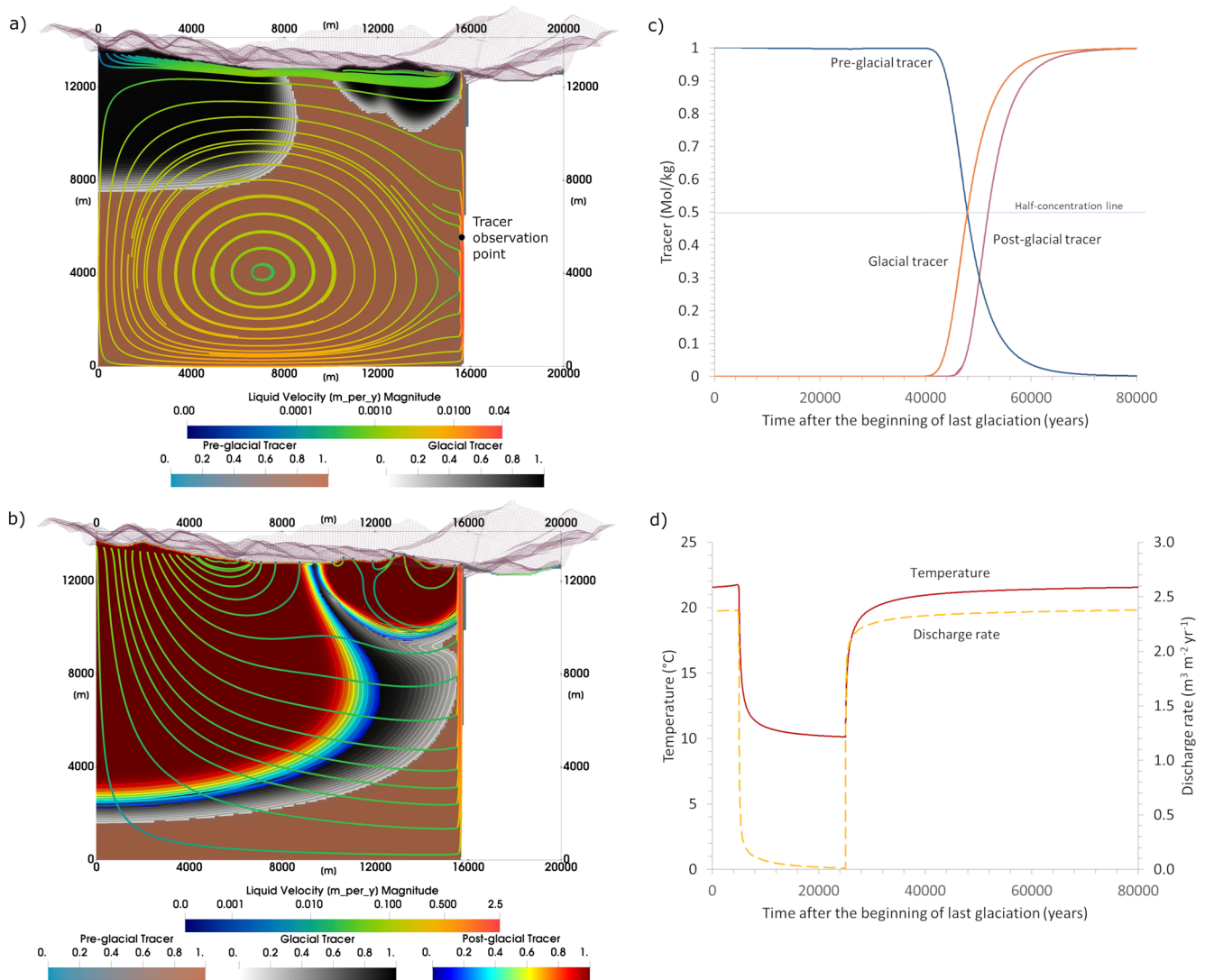| Time (years)	Event
0	Start glaciation, linear decrease in recharge. Switch from pre-glacial to glacial tracer
5,000	Start peak glaciation, recharge-starved conditions
25,000	End peak glaciation, linear increase in recharge Switch from glacial to post-glacial tracer
30,000	Start interglacial conditions
41,000	Present

Figure 8. Model streamlines and tracer concentrations in the fault as a function of time since the last glaciation, following the schedule of events in Table 3. (a) During peak glaciation a layered flow system is present with deep non-Rayleigh convection and shallow single-pass flow. The glacial tracer has entered the fault plane and displaced the pre-glacial tracer at shallow depth but the interface between the tracers remains quasi-stationary as long as there is insufficient recharge to drive single-pass flow to the bottom of the fault. (b) After onset of the current interglacial period, the post-glacial tracer displaces the pre-/glacial tracers which now discharge in the spring water at Grimsel Pass. (c) Monitoring the breakthrough of tracers at an observation point within the upflow zone below the depth of shallow groundwater flow (see panel a) reveals the sequence of events: Upflow through the conduit (yellow dashed line) ceases during peak glaciation (i.e., the discharge rate is zero). The flow pattern in the fault plane is that of panel (a) Fluid upflow increases at 25,000 years and remains constant after 30,000 years. The present is at 41,000 years. Up until about 50,000 years, some 10,000 years into the future, the spring water composition is still dominated by the pre-glacial and glacial tracers. (d) Evolution of temperature and discharge rate at the depth of the tunnel, indicating that at present (41,000 years) both temperature and discharge rate have not yet quite recovered to pre-glacial levels.

tracers remains quasi-stationary in the fault plane during the entire period of glaciation. Discharge through the conduit responds rapidly and decreases to near zero (Figure 8d).

When recharge picks up again during the transition to the current interglacial period, the system switches back to deep single-pass flow and the postglacial tracer starts to displace the glacial tracer (Figure 8b). The model spring water 11,000 years after the last glaciation (i.e., representing today's conditions) is composed of the two tracers (pre-glacial and glacial) that infiltrated the system before the last glaciation (Figure 8c). The water sampled in the upper conduit will have the signature of the pre-glacial period.

From this follows that the residence times in Table 2 in fact represent the breakthrough time of the postglacial tracer, that is, a tracer infiltrating the fault at the beginning of the current interglacial period. If the current interglacial

period started some 11,000 years ago, the fault permeability has to be in the range 1e−15 m^2–2.5e−15 m^2 to have old, pre-glacial water discharging from the springs today (note that for k_{fault} = 2.5e−15 m^2 the residence time is 10,670 years). This permeability range is in perfect agreement with permeabilities estimated from other constraints.

The simulations presented above show that real data can be reproduced with a single, internally consistent model (a model with the same geometry, initial conditions, boundary conditions and parameterization), even though the model presented here is based on simplifying assumptions. For instance, the aperture of the fault is assumed to be a uniform 100 m along the plane. In reality the width of the Grimsel fault varies along strike (Belgrano et al., 2016), affecting the cross-sectional area available for flow and hence impacting on the flow regime in the fault. Also, because the Rayleigh number depends on the aperture and depth of the fault (e.g., Lopez & Smith, 1995), it is possible that by decreasing the fault aperture, the estimated range of fault permeabilities will shift toward higher permeabilities and vice versa. However, irrespective of these uncertainties, the general conclusion of this study is that all observational constraints in the Grimsel system are consistent with subcritical single-pass flow. This conclusion is compatible with the work on the orogenic geothermal system in the Têt Valley of the Pyrenees by Taillefer et al. (2017, 2018), who estimated fault permeabilities to be on the order of 1e−14 m^2 but likewise inferred slightly subcritical flow conditions. Actual permeability measurements on large faults tend to be of similar order of magnitude (i.e., around 1e−14 m^2) or in some cases even higher (e.g., Boles et al., 2010; Bredehoeft, 1997; Screaton et al., 2000). However, permeability measurements are often carried out at relatively shallow depths where near-surface exhumation fractures may be prevalent and spatial variability of several orders of magnitude is not uncommon (e.g., Morin et al., 1998).

The unusual location of the Grimsel thermal springs underneath a mountain pass underscores the high permeability contrast between the fault plane and its host rock, allowing focused flow within the fault over tens of kilometers. Without this contrast, groundwater flow would follow the regional hydraulic gradient and drain into the Rhône Valley as shown in Figure 3. This conclusion from field observations is consistent with our simulation results, which require hydraulically tight host rocks to achieve flow conditions in the fault that are below the critical Rayleigh number.

We have assumed spatially and temporally homogeneous rock properties throughout the fault plane, although in reality the distribution of porosity and permeability is known to be heterogeneous. As noted in Section 2, earthquakes in the vicinity of Grimsel Pass suggest that segments of the fault down to 10–12 km depth may be undergoing intermittent strike-slip displacement, which presumably modifies the local porosity and permeability of the fault plane with time. Unfortunately, the location and magnitude of these modifications cannot be quantified and hence their influence cannot be simulated realistically. However, the effects of spatial heterogeneity on the flow system can be illustrated by means of simple scoping calculations using stochastic permeability fields generated with GSTools (Müller & Schüler, 2019), using a log-normal distribution of permeability around different means. As an example, the result for a mean permeability of 2.5e−15 m^2 and a short correlation length of <100 m (i.e., cell-by-cell randomized permeabilities) is shown in Figure 9. Even if the permeability of the fault is thus perturbed by internal heterogeneity, the single-pass flow pattern remains robust. The most notable effect of heterogeneity is that of flow channeling. Ingress into the upflow conduit is no longer evenly distributed along the vertical length of the conduit as in Figure 4 but occurs at discrete depth intervals. The scoping calculations show that channeling has little impact on the temperature and mixing ratios at tunnel depth. For the case shown in Figure 9, the upwelling geothermal endmember water has a temperature of 30°C, similar to the temperature when permeability is homogeneous at 2.5e−15 m^2 (Figure 6). However, the impact on the discharge temperature tends to increase with increasing correlation length of the fault permeability.

An interesting aspect of internal heterogeneity in the fault plane not shown here is that by increasing the permeability correlation length, the critical Rayleigh number may be exceeded locally and hence convection cells may form in localized regions of higher permeability. Such regions of small-scale convective circulation could have an impact on fluid residence times if fluid aliquots become trapped within a cell. Higher flow velocities within those regions could lead to local anomalies in water/rock ratios and geochemical alteration.

Clearly, our assumption of homogeneous permeabilities in the model is a simplification of reality: internal heterogeneity, anisotropy and/or a depth-dependent permeability would affect the geometry of the flow pattern, the distribution of water/rock ratios and hence the temperature and chemical overprinting of the rock and the circulating fluid. A more thorough discussion of the effect of internal heterogeneity is beyond the scope of the work
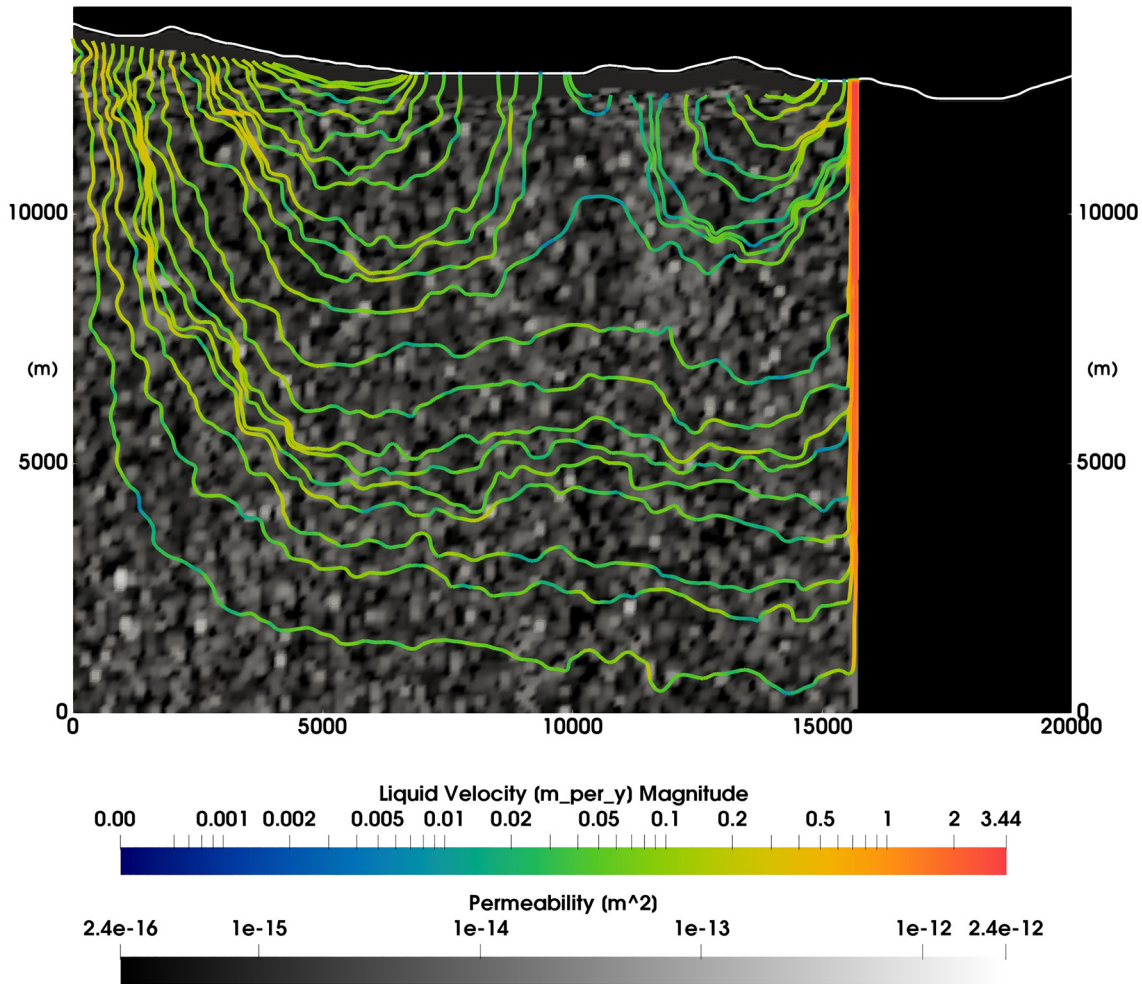
Figure 9. Flow pattern in a fault plane with heterogeneous permeability showing the effect of flow channeling while the single-pass flow pattern remains robust. Tracked fluid aliquots are released into the flow system at equally spaced sources along horizontal lines in recharge areas. Average permeability of the fault is $2.5e-15 \, m^2$. Topography is shown as white line.

presented here. The impact of flow channeling due to heterogeneity on mineral alteration in the fault plane and on the chemical signature in the spring water will be addressed in greater detail in a follow-up paper.

6. Conclusion

Recent studies of the orogenic geothermal system hosted by the GBF have provided numerous observational and modeling constraints that enable investigation of its thermal–hydraulic dynamics through numerical simulations. Water is known to ascend along a permeable, subvertical breccia zone that links adjacent fault segments. This linkage zone intersects the tunnel underneath Grimsel Pass where the water discharges as thermal springs (Belgrano et al., 2016; Hofmann et al., 2004). The geochemistry of the spring water shows that it derived from meteoric water more than 30,000 years ago, and that it penetrates to depths exceeding 10 km (Diamond et al., 2018) where it is heated to temperatures normally found in hydrothermal systems associated with active volcanism.

Our numerical simulations show that flow within the Grimsel fault is single-pass and driven by the regional topography. Recharge at high altitude some 15 km to the west of Grimsel Pass drives the meteoric water to model depths exceeding 10 km where the water acquires temperatures higher than 250°C, in accord with the observational constraints.

Based on theoretical considerations, Alt-Epping et al. (2021) demonstrated that the range of possible permeabilities of such a generic fault system are limited to within one order of magnitude: $1e-15 \, m^2 - 1e-14 \, m^2$. Here, using

mixing ratios and residence times estimated from the isotope signatures of the spring water as constraints, our simulations suggest permeabilities at the lower end of this range. Calibrating the model against the temperature of the upwelling deep geothermal fluid component narrows down the permeability range to $2e-15$ m^2–$4.8e-15$ m^2. Both homogeneous and heterogeneous distributions of fault permeabilities yield stable single-pass flow within this narrow permeability window. Because deep flow is evidently confined to the fault plane, despite the deep valleys flanking Grimsel Pass, the permeability of the surrounding rock must be substantially lower than those in this permeability window, suggesting hydraulically tight and thermally conductive conditions in the bedrock.

It follows that for a constant relief of the water table (which is primarily controlled by the topography and the recharge rate) and constant fault dimensions, the efficiency at which heat is mined from deep orogenic systems depends on the permeability of the fault. Shallow zones of anomalously hot wall-rock surrounding the faults, which may be economically interesting targets for engineered geothermal systems (e.g., Wanner et al., 2019), are likely to occur at spaced discharge sites along the strike of major faults wherever damage zones have locally enhanced fault permeability.

Discharge at such permeable sites may nevertheless be intermittent, owing to fault slip and mineral precipitation altering the distribution of permeability and to the dependency of recharge rates on varying climatic conditions in glacial/interglacial cycles. In the specific case of the Grimsel Pass, the long residence time of the deep geothermal water is likely a consequence of low recharge rates during the last glaciation event in the Swiss Alps, which started some 30,000 years ago. Deep groundwater discharging at Grimsel Pass today thus infiltrated the Grimsel fault prior to the last glaciation event. This could be confirmed in the future by using alternative water-age tracers such as ^{81}Kr (Lehmann et al., 2003).

In general terms, the new simulations confirm that water penetration depths in orogenic geothermal systems depend on the horizontal distance between recharge and discharge sites. Thus, faults with longer stretches of deep connected flow have greater potential for higher discharge temperatures, and hence greater potential to create near-surface heat anomalies. However, only a fraction of the recharging water is expected to pass through the greatest depths in the flow system, thereby limiting fluxes of the hottest fluid.

Data Availability Statement

The data on which the simulations are based are available through Waber et al. (2017), Diamond et al. (2018) and Wanner et al. (2019). The input file, datafiles and steady state output of the simulation shown in Figure 4a can be downloaded at https://doi.org/10.5281/zenodo.7154080.

References

Alt-Epping, P., Diamond, L. W., Wanner, C., & Hammond, G. E. (2021). Effect of glacial/interglacial recharge conditions on flow of meteoric water through deep orogenic faults: Insights into the geothermal system at Grimsel Pass, Switzerland. *Journal of Geophysical Research: Solid Earth*, *126*, 7. https://doi.org/10.1029/2020JB021271

Aydin, A. (2000). Fractures, faults, and hydrocarbon entrapment, migration and flow. *Marine and Petroleum Geology*, *17*(7), 797–814. https://doi.org/10.1016/s0264-8172(00)00020-9

Bächler, D., Kohl, T., & Rybach, L. (2002). 3D modelling of convective flow in the Rhine Graben. *Physics and Chemistry of the Earth*, *28*(2003), 431–441. https://doi.org/10.1016/s1474-7065(03)00063-9

Balsamo, F., Bezerra, F. H. R., Vieira, M. M., & Storti, F. (2013). Structural control on the formation of iron-oxide concretions and Liesegang bands in faulted, poorly lithified Cenozoic sandstones of the Paraíba Basin, Brazil. *Geological Society of America Bulletin*, *125*(5/6), 913–931. https://doi.org/10.1130/B30686.1

Belgrano, T. M., Herwegh, M., & Berger, A. (2016). Inherited structural controls on fault geometry, architecture and hydrothermal activity: An example from Grimsel Pass, Switzerland. *Swiss Journal of Geosciences*, *109*(3), 1–20. https://doi.org/10.1007/s00015-016-0212-9

Bense, V. F., Gleeson, T., Bour, O., Loveless, S., & Scibek, J. (2013). Fault zone hydrogeology. *Earth-Science Reviews*, *127*, 171–192. https://doi.org/10.1016/j.earscirev.2013.09.008

Bense, V. F., & Person, M. (2006). Faults as conduit–barrier systems to fluid flow in siliciclastic aquifers. *Water Resources Research*, *42*(5), W0542. https://doi.org/10.1029/2005WR004480

Berger, A., Egli, D., Glotzbach, C., Valla, P. G., Pettke, T., & Herwegh, M. (2022). Apatite low-temperature chronometry and microstructures across a hydrothermally active fault zone. *Chemical Geology*, *588*, 120633. https://doi.org/10.1016/j.chemgeo.2021.120633

Berger, A., Mercolli, I. P., Herwegh, M., & Gnos, E. (2017). *Geological map of the Aar Massif and Tavetsch and Gotthard Nappes (1:100 000), Geological special Map 129*. Swiss Federal Office of Topography swisstopo.

Boles, J. R., Horner, S., & Garven, G. (2010). *Permeability estimate of the South Ellwood fault*. Society of Petroleum Engineers. SPEpaper #133613.10p.

Bossart, P., & Mazurek, M. (1991). Grimsel test site structural geology and water flow-paths in the migration shear zone. Nagra Technical Report NTB 91-12, 1–55.

Bredehoeft, J. D. (1997). Fault permeability near Yucca mountain. *Water Resources Research*, *33*(11), 2459–2463. https://doi.org/10.1029/97wr01710

Bruhn, R. L., Parry, W. T., Yonkee, W. A., & Thompson, T. (1994). Fracturing and hydrothermal alteration in normal fault zones. *Pure and Applied Geophysics*, *142*(3–4), 609–644. https://doi.org/10.1007/bf00876057

Caine, J. S., Evans, J. P., & Forster, C. B. (1996). Fault zone architecture and permeability structure. *Geology*, *24*(11), 1025–1028. https://doi.org/10.1130/0091-7613(1996)024<1025:fzaaps>2.3.co;2

Caine, J. S., & Minor, S. A. (2009). Structural and geochemical characteristics of faulted sediments and inferences on the role of water in deformation, Rio Grande Rift, New Mexico. *Geological Society of America Bulletin*, *121*(9–10), 1325–1340. https://doi.org/10.1130/B26164.1

Chan, M. A., Parry, W. T., & Bowman, J. R. (2000). Diagenetic hematite and manganese oxides and fault-related fluid flow in Jurassic sandstones, southeastern Utah. *AAPG Bulletin*, *84*(9), 1281–1310. https://doi.org/10.1306/A9673E82-1738-11D7-8645000102C1865D

Cheng, Y., & Renner, J. (2018). Exploratory use of periodic pumping tests for hydraulic characterization of faults. *Geophysical Journal International*, *212*(1), 543–565. https://doi.org/10.1093/gji/ggx390

Craw, D., Koons, P. O., Zeitler, P. K., & Kidd, W. S. F. (2005). Fluid evolution and thermal structure in the rapidly exhuming gneiss complex of Namche Barwa–Gyala Peri, eastern Himalayan syntaxis. *Journal of Metamorphic Geology*, *23*(9), 829–845. https://doi.org/10.1111/j.1525-1314.2005.00612.x

Diamond, L. W., Wanner, C., & Waber, H. N. (2018). Penetration depth of meteoric water in orogenic geothermal systems. *Geology*, *46*(12), 1063–1066. https://doi.org/10.1130/g45394.1

Diehl, T., Clinton, J., Cauzzi, C., Kraft, T., Kästli, P., Deichmann, N., et al. (2021). Earthquakes in Switzerland and surrounding regions during 2017 and 2018. *Swiss Journal of Geosciences*, *114*(1), 1–29. https://doi.org/10.1186/s00015-020-00382-2

Dzikowski, M., Josnin, J. Y., & Roche, N. (2016). Thermal influence of an alpine deep hydrothermal fault on the surrounding rocks. *Groundwater*, *54*(1), 55–65. https://doi.org/10.1111/gwat.12313

Egli, D., Baumann, R., Küng, S., Berger, A., Baron, L., & Herwegh, M. (2018). Structural characteristics, bulk porosity and evolution of an exhumed long-lived hydrothermal system. *Tectonophysics*, *747–748*, 239–258. https://doi.org/10.1016/j.tecto.2018.10.008

Eichhubl, P., Davatzes, N. C., & Becker, S. P. (2009). Structural and diagenetic control of fluid migration and cementation along the Moab fault, Utah. *AAPG Bulletin*, *93*(5), 653–681. https://doi.org/10.1306/02180908080

Garven, G., Appold, M. S., Toptygina, V. I., & Hazlett, T. (1999). Hydrogeologic modeling of the Genesis of carbonate lead–zinc ores. *Hydrogeology Journal*, *7*(1), 108–126. https://doi.org/10.1007/s100400050183

Grasby, S. E., Ferguson, G., Brady, A., Sharp, C., Dunfield, P., & McMechan, M. (2016). Deep groundwater circulation and associated methane leakage in the northern Canadian Rocky Mountains. *Applied Geochemistry*, *68*, 10–18. https://doi.org/10.1016/j.apgeochem.2016.03.004

Grasby, S. E., & Hutcheon, I. (2001). Controls on the distribution of thermal springs in the southern Canadian Cordillera. *Canadian Journal of Earth Sciences*, *38*(3), 427–440. https://doi.org/10.1139/e00-091

Hammond, G. E., & Lichtner, P. C. (2010). Field-scale model for the natural attenuation of uranium at the Hanford 300 Area using high performance computing. *Water Resources Research*, *46*(9), W09527. https://doi.org/10.1029/2009WR008819

Hammond, G. E., Lichtner, P. C., & Mills, R. T. (2014). Evaluating the performance of parallel subsurface simulators: An illustrative example with PFLOTRAN. *Water Resources Research*, *50*(1), 208–228. https://doi.org/10.1002/2012WR013483

Herwegh, M., Berger, A., Baumberger, R., Wehrens, P., & Kissling, E. (2017). Large-scale crustal-block-extrusion during late Alpine collision. *Scientific Reports*, *7*(1), 413. https://doi.org/10.1038/s41598-017-00440-0

Hochstein, M. P., & Yang, Z. (1995). The Himalayan geothermal belt (Kashmir, Tibet, West Yunnan). In M. L. Gupta & M. Yamano (Eds.), *Terrestrial heat flow in geothermal energy in Asia* (pp. 331–368). Oxford and IBH Publishing.

Hofmann, B. A., Helfer, M., Diamond, L. W., Villa, I. M., Frei, R., & Eikenberg, J. (2004). Topography-driven hydrothermal breccia mineralization of Pliocene age at Grimsel Pass, Aar massif, central Swiss Alps. *Schweizerische Mineralogische und Petrographische Mitteilungen*, *84*, 271–302.

Ingebritsen, S. E., & Appold, M. S. (2012). The physical hydrogeology of ore deposits. *Economic Geology*, *107*(4), 559–584. https://doi.org/10.2113/econgeo.107.4.559

Ingebritsen, S. E., Sanford, W. E., & Neuzil, C. E. (2006). *Groundwater in geologic processes* (2nd ed.). Cambridge University Press. (p. 536).

Keusen, H. R., Ganguin, J., Schuler, P., & Buletti, M. (1989). Felslabor Grimsel: Geologie. Nagra Technischer Bericht NTB 87-14.

Lehmann, B. E., Love, A., Purtschert, R., Collon, P., Loosli, H. H., Kutschera, W., et al. (2003). A comparison of groundwater dating with ^{81}Kr, ^{36}Cl and ^{4}He in four wells of the Great Artesian Basin, Australia. *Earth and Planetary Science Letters*, *211*(3–4), 237–250. https://doi.org/10.1016/S0012-821X(03)00206-1

Lopez, D. L., & Smith, L. (1995). Fluid flow in fault zones: Analysis of the interplay of convective circulation and topographically driven groundwater flow. *Water Resources Research*, *31*(6), 1489–1503. https://doi.org/10.1029/95wr00422

Manning, C. E., & Ingebritsen, S. E. (1999). Permeability of the continental crust: The implications of geothermal data and metamorphic systems. *Reviews of Geophysics*, *37*(1), 127–150. https://doi.org/10.1029/1998rg900002

Maréchal, J. C., Perrochet, P., & Tacher, L. (1999). Long-term simulations of thermal and hydraulic characteristics in a mountain massif: The Mont Blanc case study, French, and Italian Alps. *Hydrogeology Journal*, *7*(4), 341–354. https://doi.org/10.1007/s100400050207

Menzies, C. D., Teagle, D. A. H., Craw, D., Cox, S. C., Boyce, A. J., Barrie, C. D., & Roberts, S. (2014). Incursion of meteoric waters into the ductile regime in an active orogen. *Earth and Planetary Science Letters*, *399*, 1–13. https://doi.org/10.1016/j.epsl.2014.04.046

Morin, R., Hickman, S., Barton, C., Shapiro, A., Benoit, R., & Sass, J. (1998). Hydrologic properties of the Dixie Valley, Nevada geothermal reservoir from well-test analyses. In *Proceedings 23rd workshop on geothermal reservoir engineering* (pp. 307–314). Stanford University.

Morrow, C., Shi, L. Q., & Byerlee, J. (1984). Permeability of fault gouge under confining pressure and shear stress. *Journal of Geophysical Research*, *89*(B5), 3193–3200. https://doi.org/10.1029/jb089ib05p03193

Mozley, P. S., & Goodwin, L. B. (1995). Patterns of cementation along a Cenozoic normal fault: A record of paleoflow orientations. *Geology*, *23*(6), 539–542. https://doi.org/10.1130/0091-7613(1995)023<0539:pocaac>2.3.co;2

Müller, S., & Schüler, L. (2019). *GeoStat-Framework/GSTools: Reverberating red (version v1.1.0)*. Zendo. https://doi.org/10.5281/zenodo.3468230

Noetzli, J., & Phillips, M. (2019). *Mountain permafrost hydrology. Hydro-CH2018 Project*. Commissioned by the Federal Office for the Environment (FOEN). https://doi.org/10.16904/slf.1.18

Norton, D., & Knight, J. (1977). Transport phenomena in hydrothermal systems: Cooling plutons. *American Journal of Science*, *277*(8), 937–981. https://doi.org/10.2475/ajs.277.8.937

Ota, K., Möri, A., Alexander, W. R., Frieg, B., & Schild, M. (2003). Influence of the mode of matrix porosity determination on matrix diffusion calculations. *Journal of Contaminant Hydrology*, *61*(1–4), 131–145. https://doi.org/10.1016/s0169-7722(02)00139-0

Person, M., Banerjee, A., Hofstra, A., Sweetkind, D., & Gao, Y. (2008). Hydrologic models of modern and fossil geothermal systems in the great basin: Genetic implications for epithermal Au–Ag and Carlin-type gold deposits. *Geosphere*, *4*(5), 888917. https://doi.org/10.1130/GES00150.1

Pfeifer, H. R., Sanchez, A., & Degueldre, C. (1992). Thermal springs in granitic rocks from the Grimsel Pass (Swiss Alps): The late stage of a hydrothermal system related to Alpine Orogeny. In Y. K. Kharaka & A. S. Maest (Eds.), *Proceedings of Water-Rock Interaction WRI-7* (pp. 1327–1330). A.A. Balkema.

Reyes, A. G. (2015). Low-temperature geothermal reserves in New Zealand. *Geothermics*, *56*, 138–161. https://doi.org/10.1016/j.geothermics.2015.04.004

Reyes, A. G., Christenson, B. W., & Faure, K. (2010). Sources of solutes and heat in low-enthalpy mineral waters and their relation to tectonic setting, New Zealand. *Journal of Volcanology and Geothermal Research*, *192*(3–4), 117–141. https://doi.org/10.1016/j.jvolgeores.2010.02.015

Screaton, E., Carson, B., Davis, E., & Becker, K. (2000). Permeability of a decollement zone: Results from a two-well experiment in the Barbados accretionary complex. *Journal of Geophysical Research*, *105*(B9), 21403–21410. https://doi.org/10.1029/2000jb900220

Sonney, R., & Vuataz, F.-D. (2008). Properties of geothermal fluids in Switzerland: A new interactive database. *Geothermics*, *37*(5), 496–509. https://doi.org/10.1016/j.geothermics.2008.07.001

Sonney, R., & Vuataz, F.-D. (2009). Numerical modelling of alpine deep flow systems: A management and prediction tool for an exploited geothermal reservoir (Lavey-les-Bains, Switzerland). *Hydrogeology Journal*, *17*(3), 601–616. https://doi.org/10.1007/s10040-008-0394-y

Sonney, R., & Vuataz, F.-D. (2010). Remobilisation of deep Na-Cl waters by a regional flow system in the Alps: Case study of Saint-Gervais-les-Bains (France). *Comptes Rendus Geoscience*, *342*(2), 151–161. https://doi.org/10.1016/j.crte.2009.12.011

Stober, I., & Bucher, K. (2007). Hydraulic properties of the crystalline basement. *Hydrogeology Journal*, *15*(2), 213–224. https://doi.org/10.1007/s10040-006-0094-4

Stober, I., Zhong, J., Zhang, L., & Bucher, K. (2016). Deep hydrothermal fluid–rock interaction: The thermal springs of Da Qaidam, China. *Geofluids*, *16*(4), 711–728. https://doi.org/10.1111/gfl.12190

Stöckhert, B., Brix, M. R., Kleinschrodt, R., Hurford, A. J., & Wirth, R. (1999). Thermochronometry and microstructures of quartz–A comparison with experimental flow laws and predictions on the temperature of the brittle–plastic transition. *Journal of Structural Geology*, *21*(3), 351–369. https://doi.org/10.1016/s0191-8141(98)00114-x

Taillefer, A., Guillou-Frottier, L., Soliva, R., Magri, F., Lopez, S., Courrioux, G., et al. (2018). Topographic and faults control of hydrothermal circulation along dormant faults in an orogen. *Geochemistry, Geophysics, Geosystems*, *19*(12), 4972–4995. https://doi.org/10.1029/2018gc007965

Taillefer, A., Soliva, R., Guillou-frottier, L., Le Goff, E., Martin, G., & Seranne, M. (2017). Fault-related controls on upward hydrothermal flow; an integrated geological study of the Têt fault, eastern Pyrénées (France). *Geofluids*, *19*, 8190109–8190119. https://doi.org/10.1155/2017/8190109

Thiebaud, E., Gallino, S. P., Dzikowski, M., & Gasquet, D. (2010). The influence of glaciations on the dynamics of mountain hydrothermal systems: Numerical modeling of the LaLéchère system (Savoie, France). *Bulletin de la Societe Geologique de France*, *181*(4), 295–304. https://doi.org/10.2113/gssgfbull.181.4.295

Upton, P., Craw, D., Yu, B., & Chen, Y.-G. (2011). Controls on fluid flow in transpressive orogens, Taiwan and New Zealand. *Geological Society, London, Special Publications*, *359*(1), 249–265. https://doi.org/10.1144/sp359.14

Vernon, A. J., van der Beek, P. A., Sinclair, H. D., Persano, C., Foeken, J., & Stuart, F. M. (2009). Variable late Neogene exhumation of the central European Alps: Low-temperature thermochronology from the Aar Massif, Switzerland, and the Lepontine dome, Italy. *Tectonics*, *28*(5). https://doi.org/10.1029/2008tc002387

Vernon, A. J., van der Beek, P. A., Sinclair, H. D., & Rahn, M. K. (2008). Increase in late Neogene denudation of the European Alps confirmed by analysis of a fission-track thermochronology database. *Earth and Planetary Science Letters*, *270*(3–4), 316–329. https://doi.org/10.1016/j.epsl.2008.03.053

Waber, H. N., Schneeberger, R., Mäder, U. K., & Wanner, C. (2017). Constraints on evolution and residence time of geothermal water in granitic rocks at Grimsel (Switzerland). *Procedia Earth and Planetary Science*, *17*, 774–777. https://doi.org/10.1016/j.proeps.2017.01.026

Wanner, C., Diamond, L. W., & Alt-Epping, P. (2019). Quantification of deep 3D thermal anomalies in orogenic geothermal systems from surface observations: Implications for heat exploration and thermochronology. *Journal of Geophysical Research*, *124*(11), 10839–10854. https://doi.org/10.1029/2019JB018335

Wenning, Q. C., Madonna, C., de Haller, A., & Burg, J. P. (2018). Permeability and seismic velocity anisotropy across a ductile–brittle fault zone in crystalline rock. *Solid Earth*, *9*(3), 683–698. https://doi.org/10.5194/se-9-683-2018

Wintsch, R. P., Christoffersen, R., & Kronenberg, A. K. (1995). Fluid–rock reaction weakening infault zones. *Journal of Geophysical Research*, *100*(B7), 13021–13032. https://doi.org/10.1029/94jb02622

Ziegler, M., Loew, S., & Moore, J. R. (2013). Distribution and inferred age of exfoliation joints in the Aar Granite of the central Swiss Alps and relationship to Quaternary landscape evolution. *Geomorphology*, *201*, 344–362. https://doi.org/10.1016/j.geomorph.2013.07.010